IEEE Access
Multidisciplinary | Rapid Review | Open Access Journal

Received December 29, 2020, accepted January 6, 2021, date of publication January 13, 2021, date of current version January 22, 2021.

Digital Object Identifier 10.1109/ACCESS.2021.3051421

Application of Physical Function Model to State Estimations of Nonlinear Mechanical Systems

HEISEI YONEZAWA[1], ITSURO KAJIWARA[1], SHOTA SATO[2], CHIAKI NISHIDOME[3], TAKASHI HATANO[2], AND SHIGEKI HIRAMATSU[2]

[1]Division of Human Mechanical Systems and Design, Hokkaido University, Sapporo 060-8628, Japan
[2]Integrated Control System Development Division, Mazda Motor Corporation, Hiroshima 730-8670, Japan
[3]CATEC Inc., Taito-ku, Tokyo 110-0016, Japan

Corresponding author: Itsuro Kajiwara (ikajiwara@eng.hokudai.ac.jp)

This work was supported in part by the Japan Society for the Promotion of Science, Grants-in-Aid for Scientific Research, under Grant JP 20J11084.

ABSTRACT The physical function model has been effectively used for model-based development (MBD) of automobile systems. This research demonstrates a novel application of this modeling method to the state estimation of nonlinear mechanical systems based on the Kalman filtering theory. The physical function model is a block diagram that describes each engineering field by a common rule, which focuses on the energy flow. Compared to traditional modeling approaches, this model has the flexibility to incorporate a wide range of nonlinear characteristics and the know-how accumulated by the manufacturers. Hence, it has a quite high affinity with the industrial world. The purpose of this research is to pioneer a new application of the physical function model beyond simulation analysis. In particular, physical function modeling offers a model of a system with multiple nonlinearities in the form of a time-varying linear state equation. By focusing on this feature, this study applies it to the Kalman filtering theory. The proposed approach is applicable to a wide range of nonlinearities, reduces the calculation load, and considers the background of the current MBD. Finally, verifications using an experimental apparatus, which simplifies an automotive drivetrain with backlash, demonstrate the effectiveness of the proposed approach.

INDEX TERMS Automotive drivetrain, backlash, block diagram, modeling, nonlinear mechanical system, physical function model, state estimation.

I. INTRODUCTION

In recent years, model-based development (MBD), which builds models of products and advances the development process by simulation analysis, has become indispensable for efficiency and high performance in industry, especially automobile manufacturing. Although modeling that satisfies the following requirements [1] is crucial for successful MBD, realizing these requirements is difficult by traditional approaches [2]–[5] such as CAD models and the finite element method:

1. A model that can describe and integrate the theories and laws by common principles and rules is necessary because mechanical systems such as automobiles are multi-sectoral complex systems that include many different engineering fields ranging from mechanics, electrical engineering, fluid mechanics, and thermal engineering. This is difficult for traditional models because they employ different approaches to different engineering fields.
2. A model that addresses multiple nonlinearities collectively while utilizing the accumulated resources in each manufacturer flexibly and universally is necessary. Mechanical systems are affected by multiple nonlinear characteristics, and each manufacturer has accumulated its own knowledge and database about the nonlinearities through experiments and so on in the process of MBD. Since traditional modeling approaches are based on linear theory, they cannot handle characteristic diagrams, experimental formulas, and statistical data acquired in actual development sites.
3. It is necessary to combine traditional approaches with a new method of modeling products according to the required functions without being restricted by the structure and shape at the planning stage. In traditional approaches, models are completed and their performances can be analyzed only after the mechanical structures, shapes, and dimensions of all parts have

The associate editor coordinating the review of this manuscript and approving it for publication was Shadi Alawneh.

been determined. Hence, they cannot handle sudden changes in planning and design. This leads to low development efficiency due to model changes.

For example, finite element (FE) modeling is well-known as a quite useful modeling method in structural engineering. Even when the FE model has some unknown parameters, it can be calibrated based on global optimization [6]. However, it is difficult to realize all of the above requirements 1, 2, and 3 by FE modeling.

On the other hand, the physical function model [7]–[9], [11], [12] has been developed to satisfy requirements 1–3. The physical function model is a block diagram where each engineering filed such as mechanics and electricity is modeled by the common description rule from the viewpoint of energy balance. By focusing on the energy flow, which is converted and transferred between the forms of heat, fluid, kinetics, and strain, this approach integrates models of different engineering fields into a common description. Specifically, two kinds of state quantities that are common to all fields are introduced: extensive quantity and intensive quantity. In the block diagram, the unified definitions of the characteristics, coefficients, and operators that are familiar to engineering fields such as an integrator are employed. Since each diagram model is standardized by the common rule, diagram models can be connected easily via the two state quantities. In addition, the model structure is roughly divided into two parts: the linear block diagram and the mechanism model. The former describes the energy flow. The latter is inserted into the linear block diagram to manipulate the numerical values of the characteristics and coefficients. The mechanism model adds the nonlinear characteristics by calculating the characteristic values from the related state quantities and substituting them in the diagram. The linear block diagram is fixed. However, the mechanism model is created independently and separately. It is subsequently integrated into the block diagram as a nesting structure. Since the mechanism model does not need to be a formulated or predetermined form, it can incorporate a wide range of multiple nonlinear characteristics into the model. This means that many different kinds of resources such as characteristic diagrams and experimental data, which are accumulated by each manufacturer, can be flexibly introduced. Another advantage of the physical function model is that it is constructed according to the required functions at the planning stage, but not its shapes and dimensions. This realizes a more general model structure. Hence, as demonstrated in the design example of a planetary gear [10], the same model diagram can be used if the functions of the product do not change regardless of design changes in its shapes or dimensions. Even when changing the functions, nonlinear characteristics, or simulation purposes, only the specific parts need to be changed. These parts can be easily replaced without affecting the functions of the other parts because the block diagram and mechanism model are formed as a nesting structure corresponding to the real parts configuration. Due to the above advantages, the physical function model has been effectively utilized mainly for MBD of automobiles. Examples include windshield wiper systems and powertrain of a passenger car [9], nonlinear mechanical systems [11], and hydraulic clutch with multiple plates, clutch with vibration absorbing mechanism, and disc brakes [12], [13]. Additionally, basic hierarchical models have been created for an engine [14] and a drivetrain [15]. In the latest application [16], the time history response and its variation of a mechanical system were analyzed based on the physical function modeling. This study [16] demonstrated the relationship between variations in the time response and the physical function model in which its each component was converted into time constant.

However, except for [17], studies on the physical function model mainly focus on simulation analysis of MBD. Few attempts to apply it to feedback control have been made. In mechanical systems, feedback control is indispensable to achieve the required functions and performances. While state quantities of a plant are necessary for closed-loop control, they are actually estimated by observers due to the limited number of measurement sensors. Because an observer is generally designed based on the plant model, this fact suggests the effective use of the physical function model, which has the affinity with the industrial world. However, few studies have investigated the applications to state estimations of mechanical systems.

Although various state estimation approaches exist, the linear Kalman filter proposed by Rudolf Kalman is the most well-known estimation method [18]–[20]. Its algorithms must be modified to apply it to nonlinear systems. These modifications include typical nonlinear Kalman filtering, the extended Kalman filter (EKF) [21], and the unscented Kalman filter (UKF) [22]. For example, the combination of EKF and recursive least square (RLS) can improve accuracy of parameter estimations for dynamical systems [23]. The application focuses on simultaneously estimating the vehicle mass and road grade for hybrid electric bus. For the development of advanced driver assistance systems, EKF and UKF enable cost-effective tracking algorithms of moving objects around road vehicles [24]. In recent years, with the rapid development of AI, machine learning-based approaches have attracted much attention for the combination with existing model-based feedback systems. As one example of such powerful approaches, a recurrent neural network (RNN) can offer an optimal predictor of the nonlinear model that can be used in the framework of UKF [25]. In addition, a fuzzy modeling approach can be combined with the EKF [26]. Other applications of EKF include mechatronic powertrains [27], a wave energy converter (WEC) [28], and positioning systems [29]. Even though both stochastic nonlinearities and multiple missing measurements are often induced in actual systems simultaneously, the novel extended Kalman filter proposed by [30] can compensate for the effects due to them, resulting in well state estimation performance. Therefore, this is an innovative observer that will cover comprehensive application situations of nonlinear mechanical systems. In general, as shown in [30], the nonlinear system needs to be linearized

by using the Taylor series expansion around the state vector to apply EKF to it. Furthermore, some comparison studies between EKF and UKF have been conducted [31], [32]. Unfortunately, EKF induces heavy calculation load when deriving the Jacobian, which is the partial differentiation of nonlinear functions with respect to states. Additionally, EKF cannot be applied to non-smooth functions such as the backlash of gears. In spite of an approach where multiple piece-wise linear systems are switched depending on the contact states in backlash [33], its application range is limited, and how to handle multiple nonlinearities is not considered. According to [31], EKF cannot also be applied for large-scale systems because of the complicated Jacobian matrix calculation. On the other hand, UKF, in which a probability density function is approximated by a Gaussian distribution, can be used to a wide range of nonlinear characteristics. The application examples include backlash systems [34], an estimation of the vehicle sideslip angle [35], robot localization approach [36], attitude determination of a spacecraft [37], and an estimation for a servo-hydraulic actuator system [38]. Although UKF has the above advantage, the calculation load tends to increase because the estimation algorithm is based on a statistical sampling method. According to [31], the calculation efficiency of UKF decreases dramatically with the increase of system scale. Additionally, since both EKF and UKF do not consider requirements 1. - 3. with respect to plant modeling, they are not always suitable estimation methods for MBD of manufacturing development sites.

The research challenges and contributions of this paper are indicated below.

- Although the physical function model has been effectively used for MBD of vehicle systems due to its usefulness, a range of the application is limited to simulation analysis. Hence, there are few investigations to apply the physical function modeling to feedback systems such as the state estimation of actual mechanical systems. Consequently, this study presents a novel application that is a combination of the physical function modeling and the Kalman filtering theory to estimate the state vector of nonlinear mechanical systems.
- EKF, which is a well-known traditional nonlinear Kalman filter, cannot be used for non-smooth (not analytic) nonlinear functions such as backlash because the Taylor expansion (Jacobian) cannot be mathematically defined. On the other hand, the Kalman filtering based on the physical function model, which is proposed in this study, can be applied to backlash systems. For a wider range of nonlinear mechanical systems, this approach allows their state quantity to be estimated. This is due to the fact that the physical function modeling expresses all of various different nonlinear systems as a time-varying linear state equation including some switching parameters.
- It is necessary to perform the experimental verifications to prove the effectiveness of the proposed method. In particular, the practicability for actual mechanical systems such as a backlash system must be demonstrated.

Considering the high affinity of the physical function model with the industrial world, the main contribution of this study is to present an application example of it to state estimations of nonlinear mechanical systems as a pioneering novel applicable field. In the proposed method, modeling of various nonlinear mechanical systems by the physical function model allows the state quantities to be estimated by a time-varying linear Kalman filter. The physical function model updates the parameters in the linear block diagram in real time by mechanism models, which are constructed from physical laws, experimental formulas, mapping, etc. in each engineering field. In other words, physical function modeling gives a model of a system with multiple nonlinearities in the form of a time-varying linear state equation. This is superior to traditional modeling approaches [2]–[5]. Compared to EKF, involving no calculations of the partial differentiation of the Jacobian reduces the calculation load in the proposed observer. Furthermore, the proposed approach, which can be applied to a wide range of nonlinear characteristics and can effectively utilize the manufacturer's resources regarding them flexibly, is in line with the current trends of product development.

This study experimentally investigates the proposed observer using a basic experimental device. The target application is a drivetrain with backlash (a dead-zone characteristic) as the main nonlinearity. In addition to the backlash, the nonlinearity of a spring force, which changes continuously, and Coulomb friction are defined as other nonlinear characteristics in the experimental device. Although the experimental device was developed considering only basic components and oscillation phenomena due to the backlash of an automobile drive system [39], [40], its structure is simplified so that a real vehicle can be abstracted. This paper regards this device as a general nonlinear mechanical system, and the effectiveness of the proposed approach is verified by the experiments.

II. BASIC EXPERIMENTAL DEVICE

A. MECHANICAL STRUCTURE

The proposed estimation method is applicable to mechanical systems with multiple nonlinearities. Figs. 1 and 2 show the basic experimental device and its dynamic model, respectively. To focus on the influence due to backlash,this device was developed so that an actual vehicle is simplified while reproducing only the basic structure of the automotive drive system [39], [40].

This model can be regarded as a three degree-of-freedom system, where the three mass points M_B, m_G, and M_E are connected with each other through stiffness and damping. Force is transferred in the one-dimensional direction upon applying the actuator thrust u_{LM}, which excites the displacement oscillations X_B, x_G, and X_E at each mass point. The nonlinear characteristic that gives the maximal influence on the oscillation is the dead-zone band of backlash created

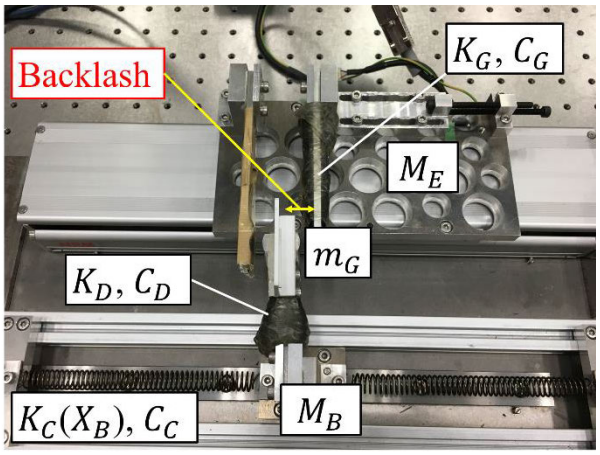

FIGURE 1. Basic experimental device.

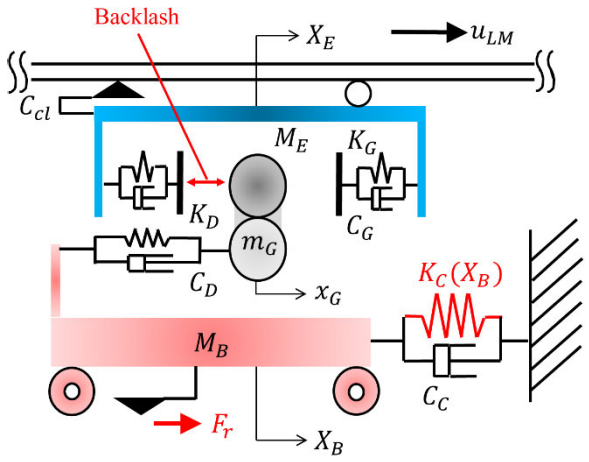

FIGURE 2. Dynamical model of the experimental device.

between M_E and m_G. This increases the vibration amplitude. In addition, it is determined that the experimental device can include other nonlinear characteristics. These are the nonlinearity of the spring constant K_C and dynamic friction force Fr generated by the translational motion of the device.

B. EXPERIMENTAL DEVICE

In the experimental device, a linear motor is used as an actuator, and the mass M_B moves on the linear guide installed in parallel with the motor (Fig. 1). M_B is connected to the walls on both sides via coil springs. Some rigid elements are reproduced by leaf springs with a damping material. The dead-zone characteristic of the backlash is created by adjusting the gap between the leaf springs K_G on both sides of the mass m_G. In this study, the motor is driven by the step thrust u_{LM}, which suddenly changes from negative to positive values. The induced oscillations (displacements and velocities) are subsequently estimated. Table 1 shows the device specifications.

TABLE 1. Parameters of the experimental device.

Symbol	Value	Symbol	Value
M_B	0.232 kg	K_G	2.7×10^4 N/m
m_G	0.039 kg	C_C	0.3 Ns/m
M_E	1.04 kg	C_D	7.5 Ns/m
K_C	660 N/m	C_G	29.0 Ns/m
K_D	1.5×10^4 N/m	C_{cl}	4.0 Ns/m

III. MODELING

A. PHYSICAL FUNCTION MODEL

This study introduces physical function modeling into the state estimation of mechanical systems. Fig. 3 shows the configuration where the basic experimental device is modeled based on physical function modeling. Table 2 shows the mathematical symbols defined in physical function model [9], [11], [12], [17]. For example, the solid black circle in Table 2 means that the signal branches in two directions in the block diagram of the physical function model. The input signal A is exactly the same physical quantity as the output signals B and C which branch from the black circle.

TABLE 2. Symbols of physical function model.

Symbol	Mathematical meaning
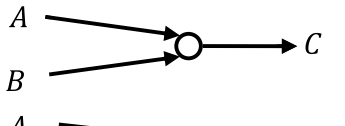	$A + B = C$
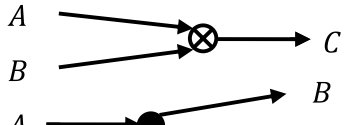	$A \times B = C$
	$A = B = C$ Branch
	$-A = B$
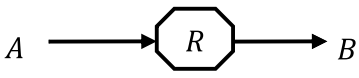	$RA = B$ R : Coefficient
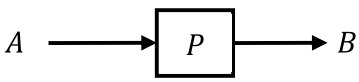	$PA = B$ P : Characteristic
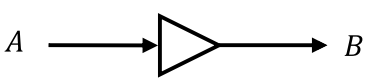	$\int A\,dt = B$
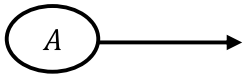	Offset

The physical function model is a block diagram where each engineering field such as mechanics and electricity is

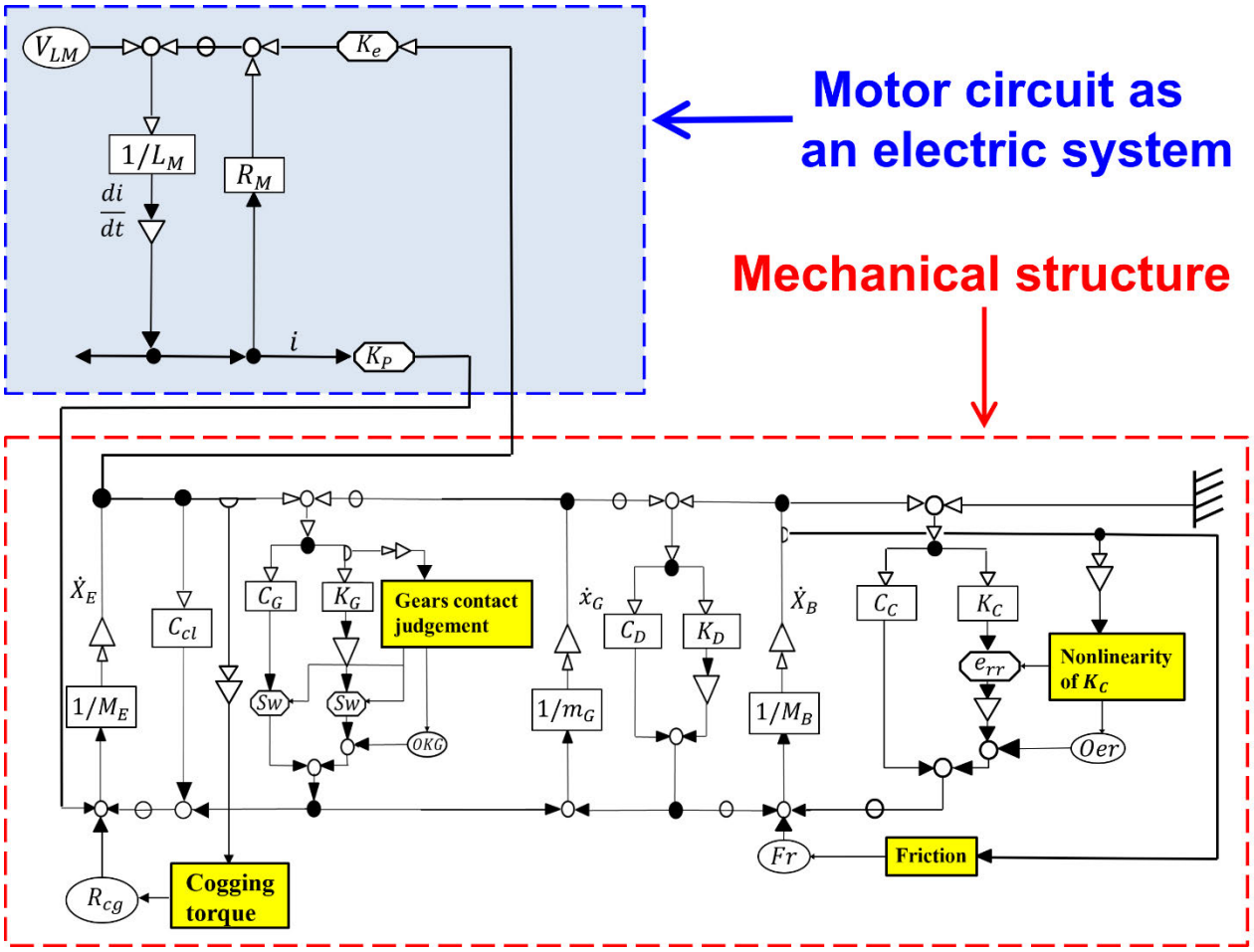

FIGURE 3. Physical function model of the nonlinear experimental device.

modeled by the common description rule focusing on energy flow. The arrows in the horizontal direction at the top and bottom of the block diagram represent two kinds of state quantities, namely "extensive quantity" and "intensive quantity," respectively. For example, they are velocity (top) and force (bottom) in Fig. 3. That is, they are a pair of physical quantities that produce power when multiplied by each other, and the block diagram describes the balance between the energy stored in the model and the energy transferred by the input/output from the outside.

See [9], [11], [12] for more details on the description of the physical function model and the meanings of each characteristic in the block diagram. The upper and lower diagrams in Fig. 3 demonstrate the motor circuit of the experimental device as an electric system and the mechanical structure shown in Fig. 1, respectively. However, because the electrical time constant of the motor is sufficiently small, the effect due to a delay is negligible [39]. Hereafter, we consider only the mechanical structure model shown in the lower diagram and omit the electric system. Since this paper demonstrates an application example of it to the Kalman filtering theory, the model should be simplified to be as low-dimensional as possible to reduce the calculation load in the digital signal processor.

In particular, this paper focuses on the feature that the physical function modeling gives a model of a system with multiple nonlinearities in the form of a time-varying linear state equation. Specifically, switching the parameters in coefficient matrices of the linear state equation expresses the nonlinear characteristics at each time step. Fig. 3 shows the two parts of the model: the block diagram described by linear equations and the mechanism model (yellow blocks) inserted to calculate the nonlinear characteristics. The mechanism model defines the nonlinearities of systems into equivalent switching parameters and calculates them in real time based on physical laws, experimental formulas, data mapping, etc. from each engineering field. Thus, the parameters are updated at each time step in the linear block diagram using methods such as substitution, addition, and multiplication.

Because the mechanism model does not need to be a formulated or predetermined form, various kinds of nonlinear characteristics can be incorporated into the model. In addition, the resources with respect to them, which are accumulated by each manufacturer, can be flexibly introduced. In the

experimental device shown in Fig. 3, the nonlinear switching parameters are Sw, OKG, e_{rr}, Oer and Fr explained later.

B. TIME-VARYING LINEAR STATE EQUATION

The following equations of motion are obtained from the physical function model shown in Fig. 3.

$$\ddot{X}_B = \frac{1}{M_B}\left\{K_D\left(x_G - X_B\right) + C_D\left(\dot{x}_G - \dot{X}_B\right) - e_{rr}K_C X_B - Oer - C_C\dot{X}_B + Fr\right\} \tag{1}$$

$$\ddot{x}_G = \frac{1}{m_G}\left\{SwK_G\left(X_E - x_G\right) + OKG + SwC_G\left(\dot{X}_E - \dot{x}_G\right) + K_D\left(X_B - x_G\right) + C_D(\dot{X}_B - \dot{x}_G)\right\} \tag{2}$$

$$\ddot{X}_E = \frac{1}{M_E}\left\{u_{LM} - C_{cl}\dot{X}_E - SwC_G\left(\dot{X}_E - \dot{x}_G\right) - SwK_G\left(X_E - x_G\right) - OKG\right\} \tag{3}$$

Thus, the time-varying linear state equation and output equation of the system are constructed as

$$\dot{x}_p = A_p x_p + B_{p1} w_p + B_{p2} u \tag{4}$$

$$y_p = C_p x_p \tag{5}$$

The observed output is composed of the displacements X_B and X_E. Each coefficient matrix is written in (6), as shown at the bottom of the page.

The output equation (5) depends on the parameter Sw. The state quantities to be estimated and the external inputs in (4) are expressed as

$$x_p = \left[X_B\ x_G\ X_E\ \dot{X}_B\ \dot{x}_G\ \dot{X}_E\right]^T \tag{7}$$

$$w_p = \begin{bmatrix} OKG \\ Oer \\ Fr \end{bmatrix}, \quad u = u_{LM} \tag{8}$$

Here, (4) and (5) are time-varying systems that include the nonlinear parameters Sw, OKG, e_{rr}, Oer and Fr in the coefficient matrices or the external input. Depending on the state quantities of the system, these are switched in real time. The calculation for each nonlinear parameter is described in the next section. It is determined that the experimental device can include the three nonlinear characteristics: dead-zone band due to the backlash (Sw and OKG), nonlinearity of the spring K_C (e_{rr} and Oer), and dynamic friction force such as that existing on the linear guide (Fr).

C. MECHANISM MODEL AND NONLINEAR SWITCHING PARAMETERS

The physical function model shown in Fig. 3 contains three mechanism models to describe the nonlinear characteristics.

The nonlinearity due to backlash in the experimental device is represented by switching the parameters Sw and OKG. Backlash produces the dead-zone characteristics. Assuming that the relative displacement between mass points M_E and m_G is ΔX, the switching rule of the nonlinear parameters and the spring force F to be transmitted are written by the following equations in the mechanism model [41], [42].

$$\begin{aligned} \Delta X &= X_E - x_G \\ F &= Sw \cdot K_G \cdot \Delta X + OKG \\ &= Sw \cdot K_G \cdot (X_E - x_G) + OKG \end{aligned}$$

$$Sw = \begin{cases} 1, & X_E - x_G > |\delta| \ \text{region(i)} \\ 1, & X_E - x_G < -|\delta| \ \text{region(ii)} \\ 0, & |X_E - x_G| \le |\delta| \ \text{region(iii)} \end{cases}$$

$$OKG = \begin{cases} -|K_G \times |\delta||, & X_E - x_G > |\delta| \ \text{region(i)} \\ |K_G \times |\delta||, & X_E - x_G < -|\delta| \ \text{region(ii)} \\ 0, & |X_E - x_G| \le |\delta| \ \text{region(iii)} \end{cases} \tag{9}$$

Note that equation (9) is not an equation obtained by some experimental measurements. According to [41], [42], this is the theoretical equation which is typically used to express

$$A_p = \begin{bmatrix} 0 & 0 & 0 & 1 & 0 & 0 \\ 0 & 0 & 0 & 0 & 1 & 0 \\ 0 & 0 & 0 & 0 & 0 & 1 \\ -\dfrac{(K_D + e_{rr}K_C)}{M_B} & \dfrac{K_D}{M_B} & 0 & -\dfrac{(C_D + C_C)}{M_B} & \dfrac{C_D}{M_B} & 0 \\ \dfrac{K_D}{m_G} & -\dfrac{(SwK_G + K_D)}{m_G} & \dfrac{SwK_G}{m_G} & \dfrac{C_D}{m_G} & -\dfrac{(SwC_G + C_D)}{m_G} & \dfrac{SwC_G}{m_G} \\ 0 & \dfrac{SwK_G}{M_E} & -\dfrac{SwK_G}{M_E} & 0 & \dfrac{SwC_G}{M_E} & -\dfrac{(SwC_G + C_{cl})}{M_E} \end{bmatrix}$$

$$B_{p1} = \begin{bmatrix} 0 & 0 & 0 \\ 0 & 0 & 0 \\ 0 & 0 & 0 \\ 0 & -\dfrac{1}{M_B} & \dfrac{1}{M_B} \\ \dfrac{1}{m_G} & 0 & 0 \\ -\dfrac{1}{M_E} & 0 & 0 \end{bmatrix}, \quad B_{p2} = \begin{bmatrix} 0 \\ 0 \\ 0 \\ 0 \\ 0 \\ \dfrac{1}{M_E} \end{bmatrix}, \quad C_p = \begin{cases} \begin{bmatrix} 1 & 0 & 0 & 0 & 0 & 0 \end{bmatrix} & (Sw = 1) \\ \begin{bmatrix} 1 & 0 & 0 & 0 & 0 & 0 \\ 0 & 0 & 1 & 0 & 0 & 0 \end{bmatrix} & (Sw = 0) \end{cases} \tag{6}$$

the dead-zone characteristic of backlash. Specifically, equation (9) expresses the nonlinear spring force due to the dead-zone characteristic of backlash shown in Fig. 4. As one example, the blue line in Fig. 4 indicates the relationship between the relative displacement ΔX and the force transmitted via spring K_G when the dead-zone width $|\delta|$ is set as 30 mm. Consequently, equation (9) can be clearly defined so that it can reproduce the non-smooth function by expressing the piecewise linear spring force for each region in Fig. 4.

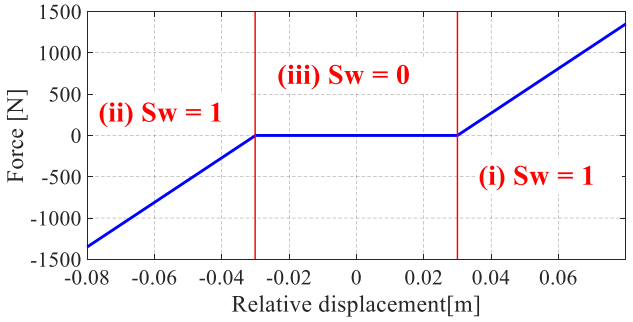

FIGURE 4. The relationship between ΔX and F.

When the relative displacement is within the dead-zone width $|\delta|$, the force is not transferred because the two mass points are not in contact with each other. On the other hand, when the relative displacement exceeds the dead-zone width, mechanical contact via the rigidity K_G occurs. Sw is a switching parameter to identify the mechanical contact, and OKG is the offset term of the spring force.

We determined that the spring rigidity K_C (nominal value: 660 N/m) of the experimental system may not be perfectly constant, and a slight (small) nonlinearity, which depends on the displacement X_B, may be included in it. Hence, the spring force due to K_C with respect to X_B is approximated by a cubic equation. In real time, the slope e_{rr} and intercept Oer, which are obtained by linearizing it, are handled as the time-varying parameters from the mechanism model.

$$\begin{aligned} F_{Kc} &= a_3 X_B^3 + a_2 X_B^2 + a_1 X_B + a_0 \\ a_0 &= 0.0303, \quad a_1 = 642.1525, \\ a_2 &= 889.0531, \quad a_3 = 1.1883 \times 10^4 \end{aligned} \tag{10}$$

By linearizing (10), the spring force F_{Kc} can be described as

$$F_{Kc} = \frac{e_{rr}}{660} \cdot X_B + Oer \tag{11}$$

$$e_{rr} = 660 \cdot (3a_3 X_B^2 + 2a_2 X_B + a_1) \tag{12}$$

$$Oer = -2a_3 X_B^3 - a_2 X_B^2 + a_0 \tag{13}$$

Through repeated a lot of the open-loop experiments in which the motor was driven by step thrust, the relational expression (10) was empirically obtained by observing their responses. In other words, the expression using the cubic equation was determined by the comparison between the response of the vehicle body displacement measured in the actual experiment and the response obtained from the simulation using the model.

The approximation using a polynomial expression is useful because of its simple form. To reduce the number of adjusting parameters (i.e. polynomial coefficients), the cubic polynomial is sufficient to retain the accuracy with the minimum coefficients.

An approach that expresses the nonlinearity of a spring force through a cubic polynomial has already been investigated in the previous research [43]. Therefore, this is a reasonable approximation method.

In the experimental device, dynamic friction force such as the seal resistance may be included on the linear guide and so on. In (14), this is theoretically modeled as the Coulomb frictional force Fr, which occurs in the opposite direction as the velocity $\dot{X}_B$. It is approximately used in the physical function model.

$$\begin{cases} Fr = |C_{rr} \cdot (M_B \times 9.8) + f_{seal}|, & \dot{X}_B < 0 \\ Fr = -|C_{rr} \cdot (M_B \times 9.8) + f_{seal}|, & \dot{X}_B > 0 \end{cases} \tag{14}$$

The values of C_{rr} and f_{seal} are 0.002 and 0.01, respectively.

Through the comparison between the response from the model in simulation and the response measured in experiment where the motor was driven by step thrust command, the nonlinear model parameters were determined by trial-and-error manual adjustments. The experimental device was developed to focus on the effect due to backlash. Therefore, when comparing the response calculated in the simulation with that observed in the experiment, those parameters were determined with more emphasis on whether the transient response induced after the backlash is traversed can be roughly reproduced.

IV. FUNCTION MODEL-BASED TIME-VARYING LINEAR KALMAN FILTER

A. EXTENDED KALMAN FILTER

To estimate the state quantities, the Kalman filtering theory is applied to the physical function models of nonlinear systems. First, a general EKF estimation algorithm is described [20]. Nonlinear functions, which are the estimation objects, are defined as

$$x_{pd}[k+1] = f_{pd}\left(x_{pd}[k]\right) + B_{pd}[k]\,u[k] + B_{pd}[k]\,v[k] \tag{15}$$

$$y_{pd}[k] = h_{pd}\left(x_{pd}[k]\right) + w[k] \quad k = 1, 2, 3, \cdots \tag{16}$$

Here, $v[k] \in \mathbb{R}^r$ is a system noise vector with a mean value of 0 and the covariance matrix Q. $w[k] \in \mathbb{R}^p$ is an observation noise vector with a mean value of 0 and the covariance matrix R. These are normal white noises, which do not depend on each other. In this study, we assumed that $v[k]$ is directly applied to the control input port. For (15) and (16), the state vector $x_{pd}[k] \in \mathbb{R}^n$ is estimated based on the observed output $y_{pd}[k] \in \mathbb{R}^p$.

In EKF, a linear approximation by a Taylor expansion around the estimated state vector is performed for the

nonlinear system. The typical linear Kalman filtering theory is subsequently applied. For the linearization, Jacobian, which is a partial differentiation of the nonlinear functions with respect to the states, must be derived. The estimation algorithm is composed of a predictive step using the model (15) and (16) and a filtering step to modify its predicted state vector based on the observed output $y_{pd}[k]$.

- Predictive step

(A priori estimate)

$$\hat{x}_{pd}^{-}[k] = f_{pd}\left(\hat{x}_{pd}[k-1]\right) + B_{pd}[k-1]\,u[k-1] \quad (17)$$

(Jacobian calculations for linearization)

$$\left.\frac{\partial f_{pd}}{\partial x_{pd}}\right|_{x_{pd}=\hat{x}_{pd}[k-1]} = A_{pd}[k-1] \quad (18)$$

$$\left.\frac{\partial h_{pd}}{\partial x_{pd}}\right|_{x_{pd}=\hat{x}_{pd}^{-}[k]} = C_{pd}[k] \quad (19)$$

(A priori covariance matrix)

$$P^{-}[k] = A_{pd}[k-1]\,P[k-1]\,A_{pd}^{T}[k-1] + B_{pd}[k-1]\,QB_{pd}^{T}[k-1] \quad (20)$$

- Filtering step

(Kalman gain)

$$g[k] = P^{-}[k]\,C_{pd}^{T}[k]\left(C_{pd}[k]\,P^{-}[k]\,C_{pd}^{T}[k] + R\right)^{-1} \quad (21)$$

(Estimated state quantity)

$$\hat{x}_{pd}[k] = \hat{x}_{pd}^{-}[k] + g[k]\left\{y_{pd}[k] - h_{pd}(\hat{x}_{pd}^{-}[k])\right\} \quad (22)$$

(A posteriori covariance matrix)

$$P[k] = \left\{I - g[k]C_{pd}[k]\right\}P^{-}[k] \quad (23)$$

The linearization using the Taylor expansion cannot be directly applied to the nonlinearity in this paper. Because the backlash characteristic of the experimental device is a non-smooth function (i.e. not continuously differentiable), the Taylor expansion (18) and (19) cannot be directly calculated. In other words, this study includes the nonlinearity that is not analytic.

Consequently, this study does not apply EKF, which is shown above for just comparison with the approach proposed in the next section, to the experimental device.

B. TIME-VARYING LINEAR KALMAN FILTER BASED ON THE PHYSICAL FUNCTION MODEL

Unlike EKF, this study proposes the time-varying linear Kalman filter which is derived from the physical function model. As demonstrated in the experimental results later, this approach can be applied to the nonlinearity that is not analytic. From the physical function model, nonlinear systems are modeled in the form of a time-varying linear state equation ((4) and (5)). Using the coefficient matrices of the state equation allows the linear Kalman filter to be directly applied to a nonstationary time series. That is, physical function modeling enables the time-varying linear Kalman filter. Compared to EKF, because partial differentiation for the Jacobian is unnecessary, the proposed approach can be used for various kinds of nonlinearities including non-smooth functions such as backlash and can reduce the calculation load in real time. From the viewpoint of modeling, the advantage is that the observer can be designed considering the backgrounds 1, 2, and 3 mentioned in the Introduction. This increases the affinity with MBD in the actual industrial world.

As shown in (4) and (5), since the state equation derived from the physical function model is in the continuous-time domain, it needs to be discretized to be handled in the Kalman filter in real time. The discretization method affects the estimation accuracy and computational complexity of the proposed observer. In this study, two kinds of methods, the Euler method and zeroth order hold, are employed. Instead of the Taylor expansion of the nonlinear functions (i.e. Jacobian), the online calculations are given by using the coefficient matrices of the time-varying linear state equation as

$$A_{pd}[k-1] = \begin{cases} I + \Delta T_s A_p((k-1)\Delta T_s) & \text{(euler method)} \\ e^{A_p((k-1)\Delta T_s)\cdot\Delta T_s} & \text{(0th order hold)} \end{cases} \quad (24)$$

$$C_{pd}[k] = \begin{cases} C_p(k\Delta T_s) & \text{(euler method)} \\ C_p(k\Delta T_s) & \text{(0th order hold)} \end{cases} \quad (25)$$

The sampling period is written as ΔT_s. Regardless of whether the Taylor expansion of the nonlinear system can be computed or not, the physical function modeling transforms it into a time-varying linear state equation. At each sampling time step, discrete numerical values of the nonlinear functions are given as switching parameters in the linear state equation. These are updated in real time. Therefore, under the condition that the sampling period is sufficiently short, the non-smooth nonlinearity such as backlash can be reproduced with sufficient good accuracy in practical use. The matrix exponential included in (24) is computed by the command 'expm (expmdemo1)' prepared in MATLAB [44]. In the case of the time-varying system (4) and (5), its nonlinear switching parameters are calculated from each estimated state quantity as

$$\begin{aligned} Sw &= Sw(\hat{X}_E, \hat{x}_G) \\ OKG &= OKG(\hat{X}_E, \hat{x}_G) \\ e_{rr} &= e_{rr}(\hat{X}_B) \\ Oer &= Oer(\hat{X}_B) \\ Fr &= Fr(\hat{V}_B) \end{aligned} \quad (26)$$

Thus, the A-matrix in (24) and the offset term in (8) are determined. (25) depends on the nonlinear parameter Sw but not on the discretization method, and is given as

$$C_p(k\Delta T_s) = \begin{cases} \begin{bmatrix} 1 & 0 & 0 & 0 & 0 & 0 \end{bmatrix} & (Sw = 1) \\ \begin{bmatrix} 1 & 0 & 0 & 0 & 0 & 0 \\ 0 & 0 & 1 & 0 & 0 & 0 \end{bmatrix} & (Sw = 0) \end{cases} \quad (27)$$

Consequently, the estimation algorithm is written as
(A priori estimate): Euler method

$$\hat{x}_{pd}^{-}[k] = \left\{I + \Delta T_s A_p\left((k-1)\Delta T_s\right)\right\}\hat{x}_{pd}[k-1] + \Delta T_s \cdot \left[B_{p1}\left((k-1)\Delta T_s\right)\ B_{p2}\left((k-1)\Delta T_s\right)\right] \cdot \begin{bmatrix} w_p[k-1] \\ u[k-1] \end{bmatrix} \tag{28}$$

(A priori estimate): 0th order hold

$$\hat{x}_{pd}^{-}[k] = \left\{e^{A_p((k-1)\Delta T_s)\cdot\Delta T_s}\right\}\hat{x}_{pd}[k-1] + \left(e^{A_p((k-1)\Delta T_s)\cdot\Delta T_s} - I\right)A_p\left((k-1)\Delta T_s\right)^{-1} \cdot \left[B_{p1}\left((k-1)\Delta T_s\right)\ B_{p2}((k-1)\Delta T_s\right] \cdot \begin{bmatrix} w_p[k-1] \\ u[k-1] \end{bmatrix} \tag{29}$$

(A priori covariance matrix): Euler method

$$P^{-}[k] = \left\{I + \Delta T_s A_p\left((k-1)\Delta T_s\right)\right\}P[k-1] \cdot \left\{I + \Delta T_s A_p\left((k-1)\Delta T_s\right)\right\}^T + (\Delta T_s)^2 \cdot \left[B_{p1}((k-1)\Delta T_s)\ \ B_{p2}((k-1)\Delta T_s)\right] \cdot Q \begin{bmatrix} B_{p1}^T((k-1)\Delta T_s) \\ B_{p2}^T((k-1)\Delta T_s) \end{bmatrix} \tag{30}$$

(A priori covariance matrix): 0th order hold

$$P^{-}[k] = \left\{e^{A_p((k-1)\Delta T_s)\cdot\Delta T_s}\right\}P[k-1]\left\{e^{A_p((k-1)\Delta T_s)\cdot\Delta T_s}\right\}^T + \left(e^{A_p((k-1)\Delta T_s)\cdot\Delta T_s} - I\right)A_p\left((k-1)\Delta T_s\right)^{-1} \cdot \left[B_{p1}\left((k-1)\Delta T_s\right)\ B_{p2}\left((k-1)\Delta T_s\right)\right] \cdot Q \begin{bmatrix} B_{p1}^T\left((k-1)\Delta T_s\right) \\ B_{p2}^T\left((k-1)\Delta T_s\right) \end{bmatrix} \cdot \left\{\left(e^{A_p((k-1)\Delta T_s)\cdot\Delta T_s} - I\right)A_p\left((k-1)\Delta T_s\right)^{-1}\right\}^T \tag{31}$$

(Kalman gain)

$$g[k] = P^{-}[k]\,C_{pd}^T[k]\left(C_{pd}[k]\,P^{-}[k]\,C_{pd}^T[k] + R\right)^{-1} = P^{-}[k]\,C_p^T(k\Delta T_s) \times \left(C_p(k\Delta T_s)P^{-}[k]\,C_p^T(k\Delta T_s) + R\right)^{-1} \tag{32}$$

(Estimated state quantity)

$$\hat{x}_{pd}[k] = \hat{x}_{pd}^{-}[k] + g[k]\left\{y_{pd}[k] - C_p(k\Delta T_s)\hat{x}_{pd}^{-}[k]\right\} \tag{33}$$

(A posteriori covariance matrix)

$$P[k] = \left\{I - g[k]\,C_{pd}[k]\right\}P^{-}[k] = \left\{I - g[k]\,C_p(k\Delta T_s)\right\}P^{-}[k] \tag{34}$$

Here, the covariance matrix of observation noise R and the observed output $y_{pd}[k]$ are defined as

$$R = \begin{cases} r \times I_{1\times 1} & (Sw = 1) \\ r \times I_{2\times 2} & (Sw = 0) \end{cases} \tag{35}$$

$$y_{pd}[k] = \begin{cases} X_B(n\Delta T_s) & (Sw = 1) \\ \begin{bmatrix} X_B(n\Delta T_s) \\ X_E(n\Delta T_s) \end{bmatrix} & (Sw = 0) \end{cases} \tag{36}$$

corresponding to (27). In the experiments below, the covariance matrices were adjusted as $Q = q \times I_{4\times 4} = 10^8 \times I_{4\times 4} \sim 10^9 \times I_{4\times 4}$ and $r = 10^0 \sim 10^1$. Sampling periods of the experimental verifications with zeroth order hold and Euler method were 0.42 ms and 0.34 ms, respectively.

V. EXPERIMENTS

A. VERIFICATION CONTENTS

This study verifies the proposed method experimentally. Two kinds of Kalman filters are investigated depending on the discretization method for the physical function model. One involves the Euler method and the other involves the zeroth order hold. Moreover, additional verifications give a uniformly distributed noise of 10% to the observed output to confirm the robustness of the proposed method. In summary, a total of four verifications (two kinds of discretization × the presence or absence of noise) were performed. All of the experimental results are shown in a table in the form of mean square error (MSE) [38] with respect to each state quantity. These performances can be quantitatively evaluated.

B. EXPERIMENTAL SYSTEM

Figure 5 shows the experimental system. Figure 5 (a) is the configuration of the feedback system (conceptual scheme). Figure 5 (b) overviews the real experimental system.

In Fig. 5 (a), the motor is driven by the thrust command signal, which is amplified by the servo amplifier. To clearly evaluate the effects due to backlash, a step signal, which suddenly changes from negative to positive values at 2.0 s, is given as the thrust command. The three displacements in (7) are measured by laser displacement sensors (LDS: KEYENCE, IL-300). The velocities, which are the state variables in (7), are obtained by differentiating the sensor signals. The observed output (36) of the measured displacements by the sensors is fed back to the digital signal processor (DSP: mtt, iBIS, DSP7101A). According to this observed output, the Kalman filter in DSP estimates the state variables. As the observation noise, random number values are added to the sensor signal in DSP.

C. VERIFICATION RESULTS

Figs. 6 - 11 show the experimental results without the observation noise. Figs. 6, 7, and 8 show the three displacements X_B, x_G, and X_E, respectively. Figs. 9, 10, and 11 show the three velocities V_B, v_G, and V_E, respectively.

Next, the results obtained by the experimental verifications in which a uniformly distributed noise of 10% was given to the observed output (sensor signal) are demonstrated below.

Figs. 12 - 17 show the verification results obtained by the experiments with the observation noise. Figs. 12, 13, and 14 show the three displacements X_B, x_G, and X_E, respectively.

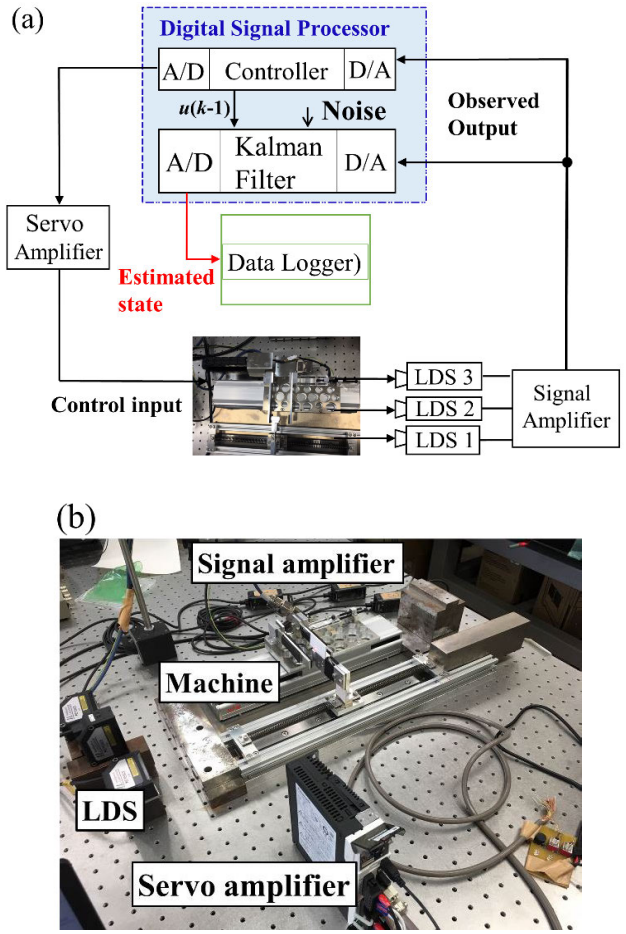

FIGURE 5. Experimental system. (a) System diagram and (b) overview of the real experimental system.

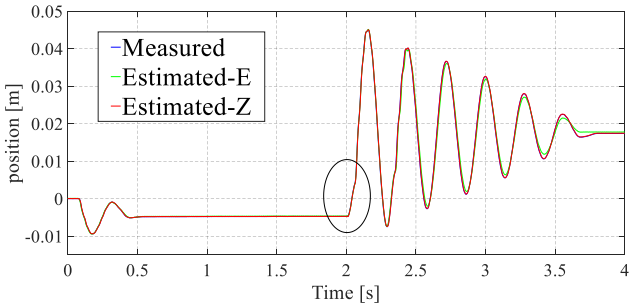

FIGURE 6. Measured and estimated displacements of the mass M_B to experimentally verify the estimation accuracy. The blue line shows the signal obtained from the sensor. The red and green lines show the results estimated by the proposed Kalman filters with the zeroth-order hold and the Euler method, respectively.

Figs. 15, 16, and 17 show the three velocities V_B, v_G, and V_E, respectively.

In each graph, the red (Estimated-Z) and green (Estimated-E) lines show the results estimated by the Kalman filters with the zeroth-order hold and the Euler method, respectively. The blue line indicates the true value obtained from the sensor. Table 3 shows the MSEs with respect to each estimated state quantity.

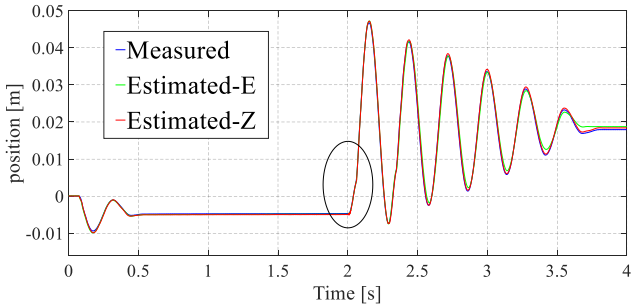

FIGURE 7. Measured and estimated displacements of the mass m_G to experimentally verify the estimation accuracy. The blue line shows the signal obtained from the sensor. The red and green lines show the results estimated by the proposed Kalman filters with the zeroth-order hold and the Euler method, respectively.

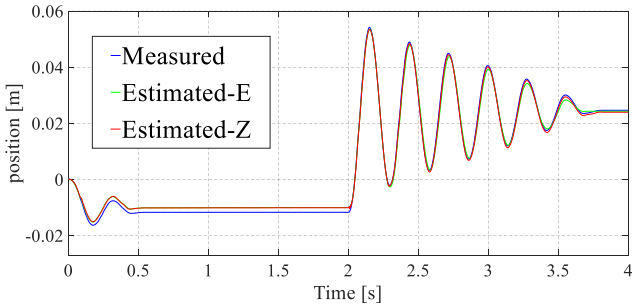

FIGURE 8. Measured and estimated displacements of the mass M_E to experimentally verify the estimation accuracy. The blue line shows the signal obtained from the sensor. The red and green lines show the results estimated by the proposed Kalman filters with the zeroth-order hold and the Euler method, respectively.

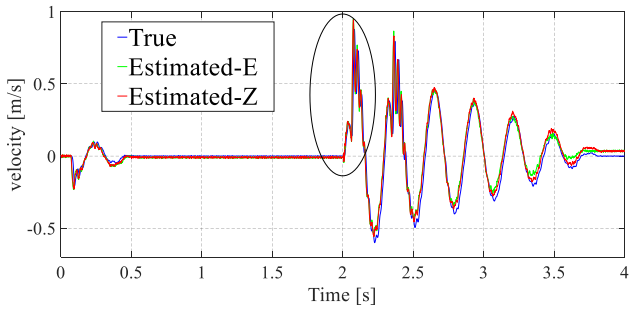

FIGURE 9. Velocities of the mass M_B demonstrating the estimation accuracy via experimental verifications. The blue line shows the value obtained from the sensor. The red and green lines show the results estimated by the proposed Kalman filters with the zeroth-order hold and the Euler method, respectively.

D. DISCUSSION

The time history responses of the displacement and velocity demonstrate the excellent estimation accuracy of the proposed method (Figs. 6 - 11). The overall trend indicates that the estimated values are almost the same as the measured (true) ones, meaning that the state quantities were properly estimated. Moreover, the remarkably small values of mean square errors (MSE) with respect to each state quantity shown in Table 3 confirm the effectiveness of the proposed approach.

Figs. 12-17 indicate that each state variable was successfully estimated even though the observation noise was given

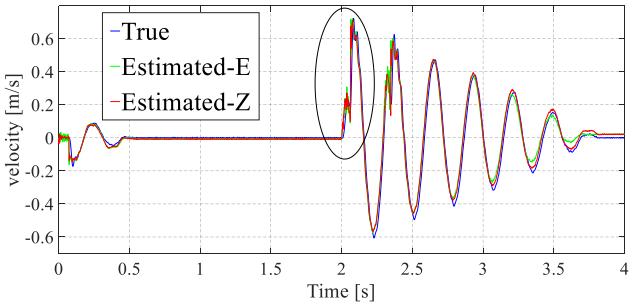

FIGURE 10. Velocities of the mass m_G demonstrating the estimation accuracy via experimental verifications. The blue line shows the value obtained from the sensor. The red and green lines show the results estimated by the proposed Kalman filters with the zeroth-order hold and the Euler method, respectively.

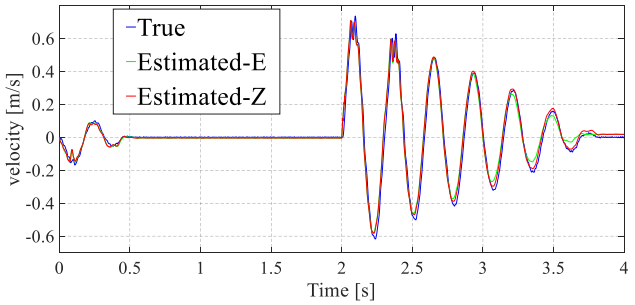

FIGURE 11. Velocities of the mass M_E demonstrating the estimation accuracy via experimental verifications. The blue line shows the value obtained from the sensor. The red and green lines show the results estimated by the proposed Kalman filters with the zeroth-order hold and the Euler method, respectively.

TABLE 3. Experimental results of the mean squared errors on each state variable.

State quantity	MSE (zeroth-order hold)	MSE (Euler method)	MSE (zeroth-order hold, with noise)	MSE (Euler method, with noise)
$\hat{X}_B$	4.325 $\times 10^{-8}$	2.921 $\times 10^{-8}$	2.564 $\times 10^{-7}$	2.104 $\times 10^{-7}$
$\hat{x}_G$	1.603 $\times 10^{-7}$	1.940 $\times 10^{-7}$	5.573 $\times 10^{-7}$	5.563 $\times 10^{-7}$
$\hat{X}_E$	1.421 $\times 10^{-6}$	1.023 $\times 10^{-6}$	6.726 $\times 10^{-7}$	5.577 $\times 10^{-7}$
$\hat{\dot{X}}_B$	0.0034	0.0038	0.0050	0.0055
$\hat{\dot{x}}_G$	0.0015	0.0016	0.0025	0.0028
$\hat{\dot{X}}_E$	0.0012	0.0012	0.0020	0.0019

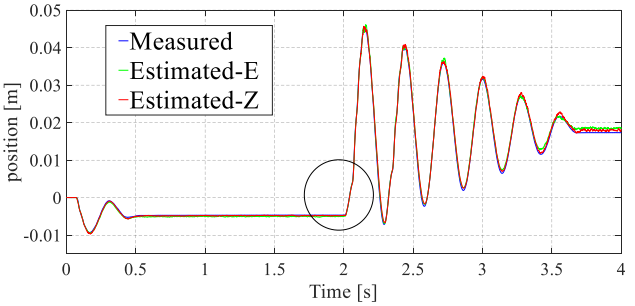

FIGURE 12. Displacements of the mass M_B obtained by the experiments with observation noise 10%. The blue line shows the signal obtained from the sensor. The red and green lines show the results estimated by the proposed Kalman filters with the zeroth-order hold and the Euler method, respectively.

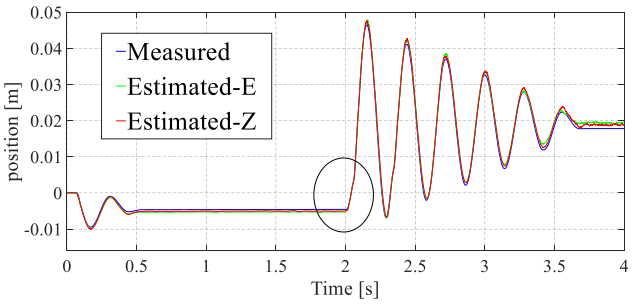

FIGURE 13. Displacements of the mass m_G obtained by the experiments with observation noise 10%. The blue line shows the signal obtained from the sensor. The red and green lines show the results estimated by the proposed Kalman filters with the zeroth-order hold and the Euler method, respectively.

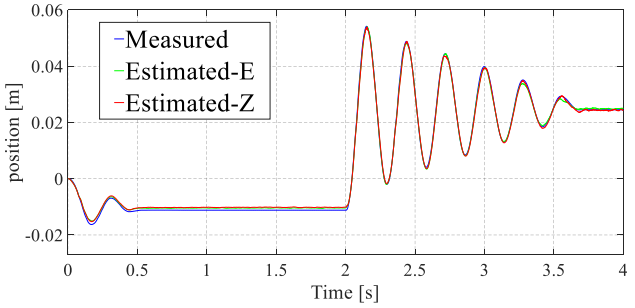

FIGURE 14. Displacements of the mass M_E obtained by the experiments with observation noise 10%. The blue line shows the signal obtained from the sensor. The red and green lines show the results estimated by the proposed Kalman filters with the zeroth-order hold and the Euler method, respectively.

in DSP. Although the effects due to the observation noise appear in some detailed parts of the velocity responses shown in Figs. 15 and 16, the macro behavior is reproduced in both the red and green lines. In the application presented in this study, while the nonlinearity of the system is addressed by the physical function modeling, the robustness against observation noise can be due to the linear Kalman filtering.

In particular, the responses from 2.0 s to 2.5 s in the displacements shown in Figs. 6, 7, 12, and 13 and the velocities shown in Figs. 9, 10, 15, and 16 confirm the validity of the mechanism model included in the physical function model presented in Fig. 3. Specifically, the nonlinearity due to backlash described by the mechanism model is clearly observed in those figures. As the motor is driven by the thrust, which suddenly changes at 2.0 s, there is a time zone in which the upstream side (mass point M_E) and the downstream side (mass points m_G and M_B) are not in contact with each other in the backlash. In other words, the experimental device is in a state of free vibration. The black circles in Figs. 6, 7, 9, 10, 12, 13, 15, and 16 indicate the nonlinear behavior induced by backlash.

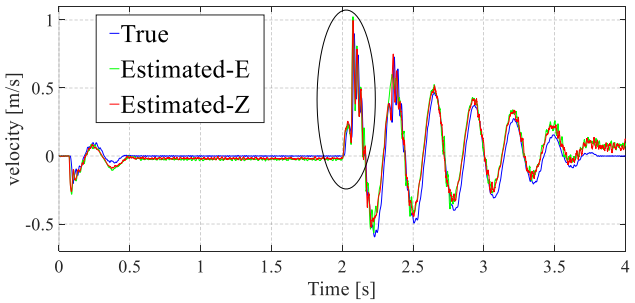

FIGURE 15. Velocities of the mass M_B obtained by the experiments with observation noise 10%. The blue line shows the value obtained from the sensor. The red and green lines show the results estimated by the proposed Kalman filters with the zeroth-order hold and the Euler method, respectively.

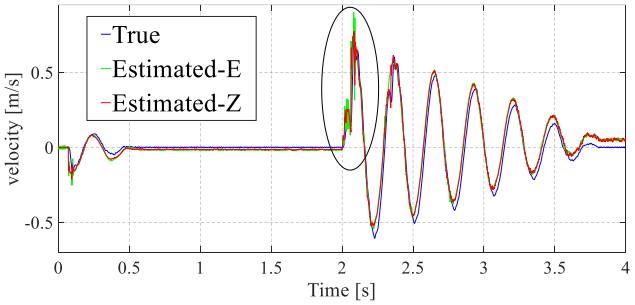

FIGURE 16. Velocities of the mass m_G obtained by the experiments with observation noise 10%. The blue line shows the value obtained from the sensor. The red and green lines show the results estimated by the proposed Kalman filters with the zeroth-order hold and the Euler method, respectively.

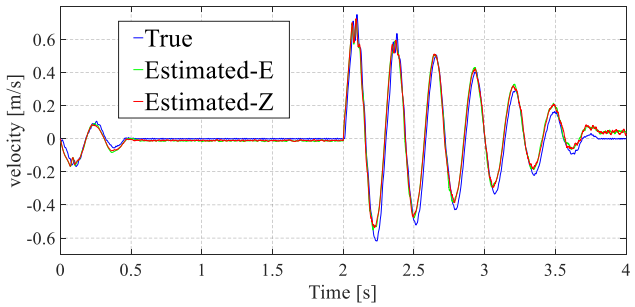

FIGURE 17. Velocities of the mass M_E obtained by the experiments with observation noise 10%. The blue line shows the value obtained from the sensor. The red and green lines show the results estimated by the proposed Kalman filters with the zeroth-order hold and the Euler method, respectively.

Figs. 18 and 19 show zooming in the curves in the key interval. Figs. 18(a), 18(b), 19(a), and 19(b) are enlarged views of Figs. 6, 7, 9, and 10, respectively, indicating the backlash characteristics estimated by the time-varying linear Kalman filter. Similarly, Figs. 20(a), 20(b), 21(a), and 21(b), which are enlarged views of Figs. 12, 13, 15, and 16, respectively, demonstrate zooming in the curves in the key interval. The arrow in Figs. 18 (a) and 20 (a) indicates the moment when the experimental device switches from a free vibration state to a forced vibration state.

Figs. 18, 19, 20, 21 show the non-smooth displacement responses and the velocity oscillations in the high-frequency

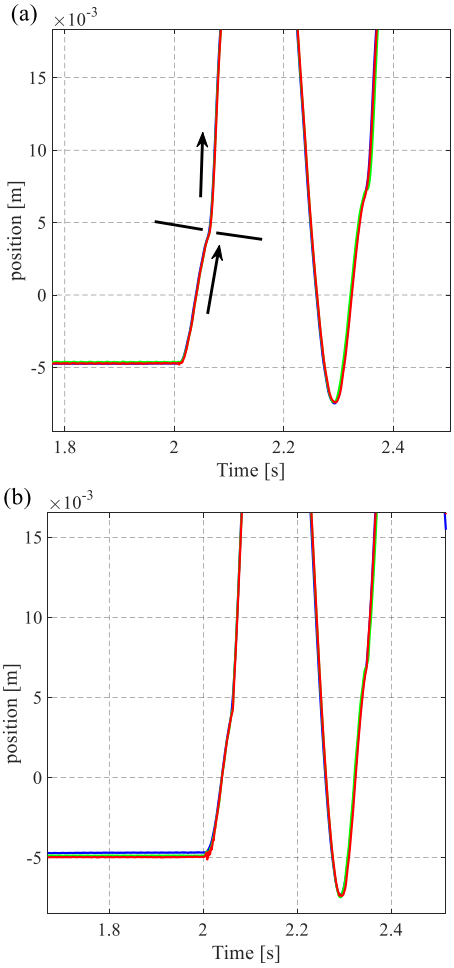

FIGURE 18. Enlarged graphs of Figs. 6 and 7, demonstrating nonlinear characteristics due to backlash.

modes. These are due to the nonlinear characteristic when the backlash condition switches from disconnected to coupled. The red and green lines of the estimated values also reproduce these responses. Consequently, the mechanism model plays an important role in the high estimation accuracy of the responses due to nonlinear characteristics when employing Kalman filtering. It is revealed from the experimental results that the proposed method is absolutely effective to estimate the states of the nonlinear system even though EKF cannot be applied to such a system including the non-smooth nonlinearity.

In this study, as indicated by the red or green line, the state equation from the physical function model is discretized by Euler method or zeroth order hold. The discretization method affects the estimation accuracy and calculation load of the proposed approach. Comparing the values of MSE in the second and third columns of Table 3, the approach with the zeroth order hold exhibits a bit higher estimation accuracy over the Euler method with respect to the two velocities $\hat{\dot{X}}_B$ and $\hat{\dot{x}}_G$. Moreover, when including observation noise, comparing MSEs in the fourth and fifth columns, the zeroth-order hold takes the smaller values with respect

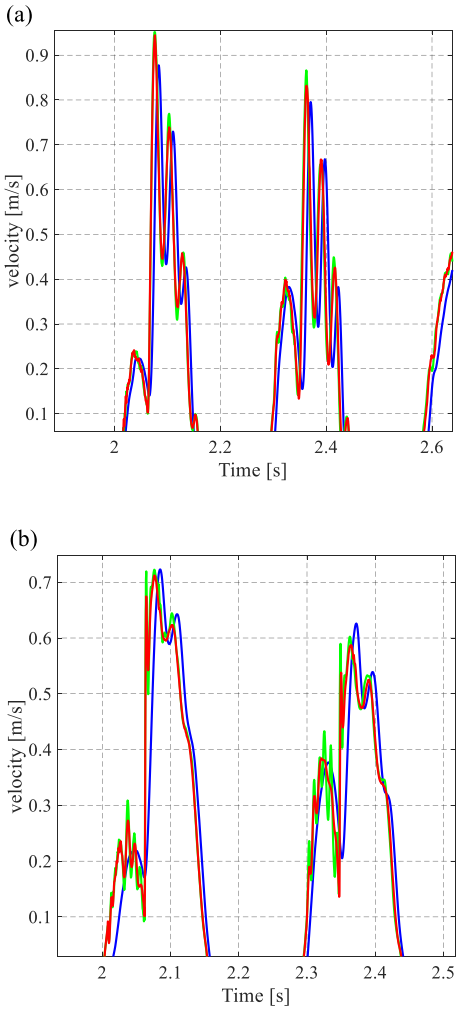

FIGURE 19. Enlarged graphs of Figs. 9 and 10, demonstrating nonlinear characteristics due to backlash.

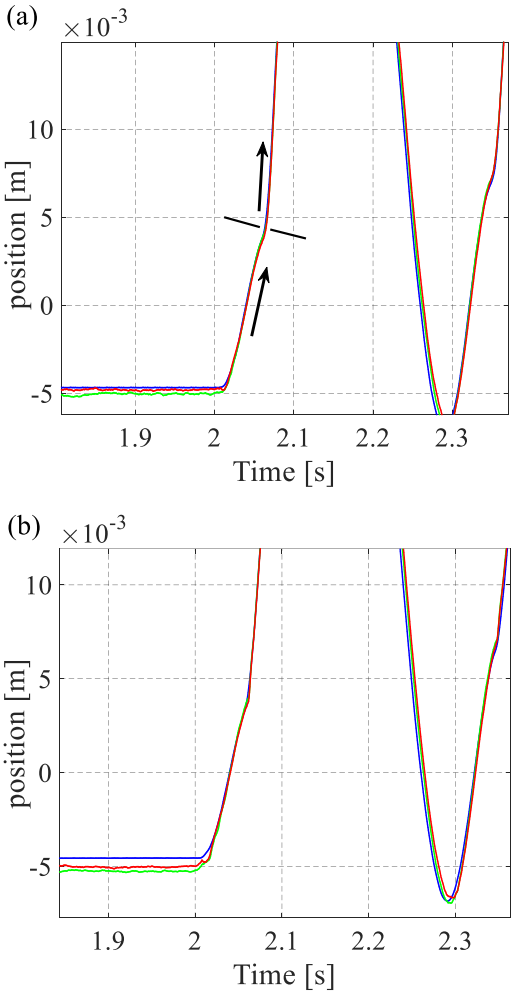

FIGURE 20. Enlarged graphs of Figs. 12 and 13, demonstrating nonlinear characteristics due to backlash.

to $\hat{\dot{X}}_B$ and $\hat{\dot{x}}_G$, in which the effect due to backlash appears directly. The overall trend of the experimental result shown in the figure on each state variable indicates that there is little difference between the two discretization methods. However, the clear performance difference between the Euler method and the zeroth-order hold can be observed from Figs. 19(b) and 21(a)(b), which demonstrate zooming in the curves in the key interval. Specifically, the green waveform obtained by the Euler method fluctuates more intensely from 2.0 s to 2.5 s. Because Figs. 18, 19, 20, and 21 show the backlash characteristics, they are regarded as the curves in the key interval. Considering practical use in the industrial world, there is a possibility that the performance differences such as those in Figs. 19(b) and 21(b) will affect the estimation accuracy of the backlash characteristics. These results imply that a higher estimation accuracy may be obtained by application of the model discretized by zeroth order hold to the Kalman filter. One of the reasons may be the difference in the calculation method between zeroth-order hold and the Euler method. Regarding the computation of the matrix exponential in (24) [44], the Euler method employs an approximation, which neglects terms of orders higher than or equal to two in the Taylor expansion. Because the oscillations in the high-frequency modes occur immediately after the backlash is traversed, the effects due to the terms with higher orders in the Taylor series may not be negligible. This may attribute to the deteriorated estimation accuracy of the Euler method. From Fig. 21(b), we can see that the time-varying linear Kalman filter with the Euler method is susceptible to the observation noise. This is because the above negative effect regarding the computation of the matrix exponential is promoted by the observation noise.

On the other hand, the Euler method is superior to the zeroth-order hold from the viewpoint of calculation load in the Kalman filter. Table 4 shows the time required to execute simulations to verify the proposed approach using different discretization methods. These results were obtained by executing a simulation program of m-file (MATLAB R2016a), which includes the commands 'tic', 'toc' for time measuring. As PC for the analysis, DELL Precision 3630 Tower (Dell Inc.; CPU; Xeon E-2124, Memory; 16GB DDR4) was used. In the simulations, sampling period ΔT_s is 0.02 ms.

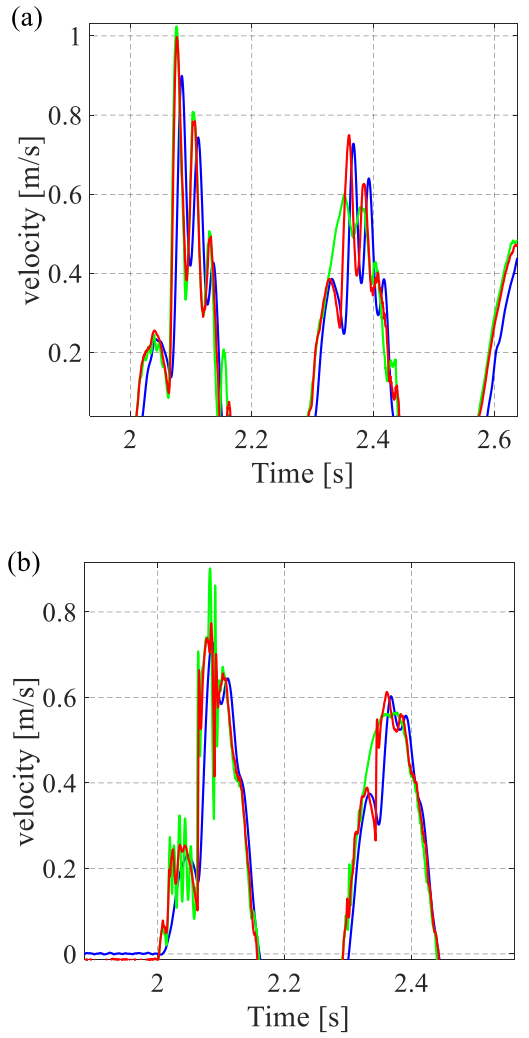

FIGURE 21. Enlarged graphs of Figs. 15 and 16, demonstrating nonlinear characteristics due to backlash.

TABLE 4. Simulation time of each discretization method measured to compare their calculation loads with each other.

Discretization method	Zeroth order hold (ΔT_s : 0.02 ms)	Euler method (ΔT_s : 0.02 ms)
Simulation times [s]	12.161340	4.932210

As shown in Table 4, it is meaningful to compare the two discretization methods because there is the great difference in their calculation loads. Comparing the two results shown in Table 4, the simulation is finished by the Euler method in less than half of the time required for that by the zeroth order hold. Hence, the approach with the Euler method has a smaller calculation load. This can also be attributed to the difference in the approximation method used to calculate the matrix exponential. Consequently, the results of this study suggest that there is a trade-off relationship between estimation accuracy and calculation load with respect to the discretization methods. Hence, it is necessary to appropriately select the discretization methods for the physical function model according to which feature (estimation accuracy or calculation load) is more important.

As discussed above, the major difficulty is that the physical function model needs to be discretized in real time in order to be applied to the Kalman filtering. This is due to the fact that the physical function model is always constructed in the continuous-time domain, which has the physical meanings explicitly. The real-time discretization sometimes makes it difficult to implement the Kalman filter on digital control systems. Therefore, the following two approaches will be important in the future. First, the discretization method itself needs to be improved. In particular, a novel discretization method, which can achieve both high calculation efficiency and good accuracy simultaneously, should be useful for the proposed estimation method. Second, the modification, which can directly offer a discrete-time-varying linear state equation without losing physical meanings in each engineering field and parts configuration in product systems, is required for the current physical function modeling.

E. ADDITIONAL EXPERIMENTS TO VERIFY THE PROPOSED ESTIMATION APPROACH WITH ONLINE SWITCHING OF DISCRETIZATION METHODS

With respect to the discretization methods for the physical function model, Table 4 suggests that the Euler method should be chosen when the high calculation efficiency online is more important. On the other hand, from Figs. 19(b) and 21(b), we can see that the zeroth-order hold provides a higher estimation accuracy of the response due to backlash.

Based on the above results, some additional experimental results are presented in this section. These additional results were obtained by the proposed estimation approach which is further modified to switch the two discretization methods in real time according to coupling conditions in backlash. Specifically, while M_E and m_G are not in contact with each other in the backlash (i.e. during the disconnecting state), the zeroth-order hold is used because the estimation accuracy of the backlash characteristic becomes more important. On the other hand, at other times, the Euler method is always applied to reduce the calculation loads. Therefore, the purpose of switching the discretization methods online in the time-varying linear Kalman filter is to utilize both the good accuracy of the zeroth-order hold and the high calculation efficiency of the Euler method.

Figs. 22-27 show the additional verification results obtained by the experiment in which the two discretization methods were switched online in the proposed estimation algorithm. Figs. 22, 23, and 24 demonstrate the time responses of the displacements X_B, x_G, and X_E, respectively. Figs. 25, 26, and 27 are the time responses of the velocities $\dot{X}_B$, $\dot{x}_G$, and $\dot{X}_E$, respectively.

In each graph, the red line indicates the result estimated by the time-varying linear Kalman filter including online

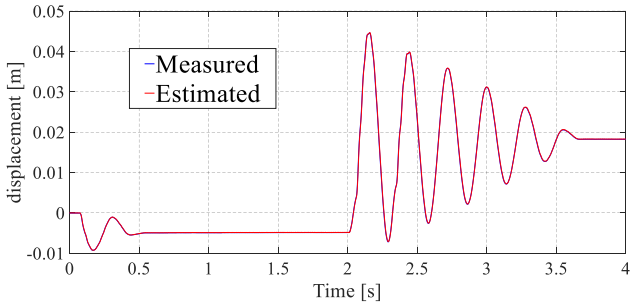

FIGURE 22. Displacement of the mass M_B obtained by the experiment in which the two discretization methods were switched in real time. The blue line shows the signal obtained from the sensor. The red line shows the result estimated by the proposed Kalman filter.

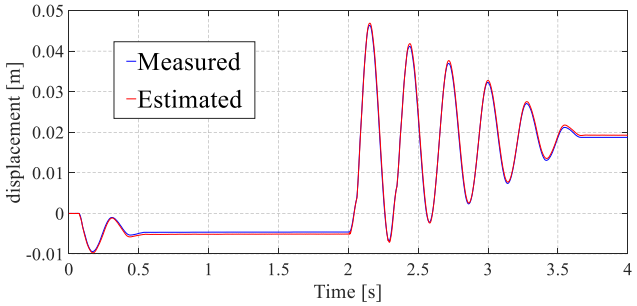

FIGURE 23. Displacement of the mass m_G obtained by the experiment in which the two discretization methods were switched in real time. The blue line shows the signal obtained from the sensor. The red line shows the result estimated by the proposed Kalman filter.

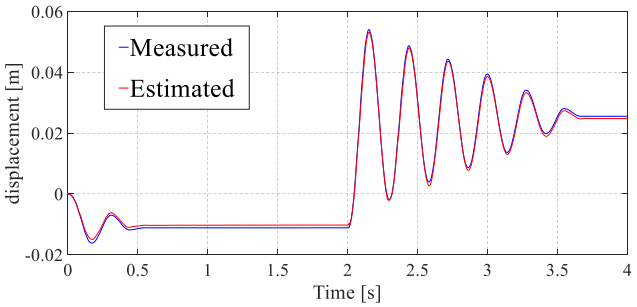

FIGURE 24. Displacement of the mass M_E obtained by the experiment in which the two discretization methods were switched in real time. The blue line shows the signal obtained from the sensor. The red line shows the result estimated by the proposed Kalman filter.

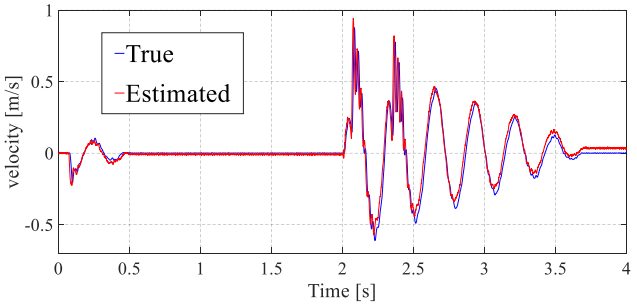

FIGURE 25. Velocity of the mass M_B obtained by the experiment in which the two discretization methods were switched in real time. The blue line shows the value obtained from the sensor. The red line shows the result estimated by the proposed Kalman filter.

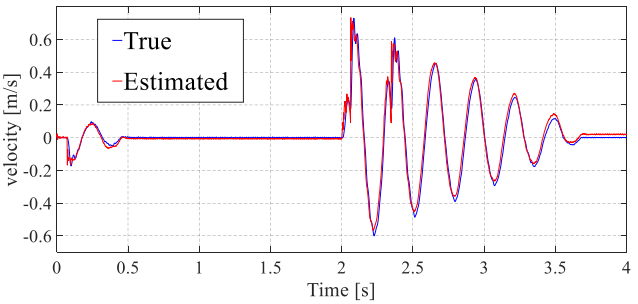

FIGURE 26. Velocity of the mass m_G obtained by the experiment in which the two discretization methods were switched in real time. The blue line shows the value obtained from the sensor. The red line shows the result estimated by the proposed Kalman filter.

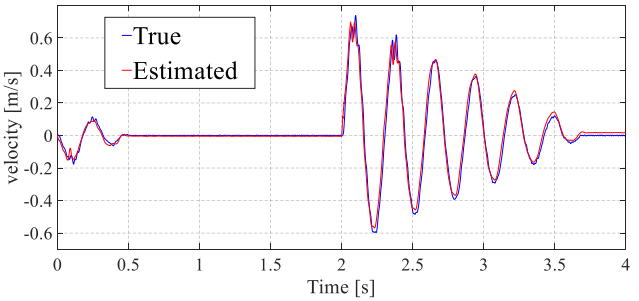

FIGURE 27. Velocity of the mass M_E obtained by the experiment in which the two discretization methods were switched in real time. The blue line shows the value obtained from the sensor. The red line shows the result estimated by the proposed Kalman filter.

switching of the discretization methods. The true value obtained from the sensor is shown in the blue line.

Figs. 22-27 demonstrate that each state variable was successfully estimated by the time-varying linear Kalman filter even when the discretization methods for the physical function model were changed online. In each figure, the red line reproduces not only the macro behavior such as the primary vibration mode at the first natural frequency 4 Hz, but also the backlash characteristic occurring from 2.0 s to 2.5 s.

Note that online calculation loads induced in the experiments of Figs. 22-27 should be less than those required for the Kalman filter employing only the zeroth-order hold. Consequently, Figs. 22-27 further verified the effectiveness of the proposed estimation approach based on the physical function model.

Despite the well performances by the modified estimation approach shown above, online switching of the discretization methods is considered to be effective for only backlash systems. This is because backlash has only two coupling conditions, leading to small number of switching the discretization methods. Therefore, as described in the end of Section 5.D., a novel discretization method, which can achieve both high calculation efficiency and good accuracy simultaneously, should be necessary for a wider range of nonlinear systems.

VI. CONCLUSION

The physical function model, which has been effectively used for MBD of vehicle systems, can be applied to the Kalman filtering theory to estimate the state of nonlinear mechanical systems. Compared to traditional modeling approaches, physical function modeling has many advantages such as the ability to flexibly express a wide range of nonlinear characteristics and to integrate models in different engineering fields. These features result in a high affinity with the industrial world. The main contribution of this study is to pioneer novel application areas of the physical function model other than simulation analysis. By focusing on the feature where nonlinear systems are modeled as a time-varying linear state equation, we present an approach for applying it to Kalman filtering. The proposed observer is applicable not only to various kinds of nonlinearities and the reduction in the calculation load, but also aligns with the background and trends of the current MBD. Finally, the high estimation performances of the present method were experimentally verified.

In the future, we plan to investigate nonlinear feedback control systems using state estimations based on the proposed approach. In addition, to more efficiently identify the parameters of the physical function model, a more theoretical and quantitative method using optimization techniques such as genetic algorithm (GA) will be necessary. This improvement of the identification method will be included in future tasks of this study.

ACKNOWLEDGMENT

The authors would like to thanks the Japan Society for the Promotion of Science for their support under Grands-in-Aid for Scientific Research Programs (KAKENHI).

REFERENCES

[1] A. Nagamatsu, S. Sumida, and S. Hiramatsu, "Concept and use of virtual product for automobile development," *Trans. Jpn. Soc. Mech. Eng., C*, vol. 69, no. 678, pp. 356–363, 2003.

[2] B. J. H. Jacobson, "On vehicle driving cycle simulation," in *Proc. Int. Congr. Expo.*, Detroit, MI, USA, SAE Rep. 950031, 1995, doi: 10.4271/950031.

[3] I. Arsie, R. Flora, C. Pianese, G. Rizzo, and G. Serra, "A computer code for S.I. engine control and powertrain simulation," *Trans.-J. Engines*, vol. 1093, pp. 935–949, SAE Tech. Paper 2000-01-0938, 2001.

[4] S. Noguchi, K. Nagasaki, S. Nakayama, T. Kanada, T. Nishino, and T. Ohtani, "Static stress analysis of link plate of roller chain using finite element method and some design proposals for weight saving," *J. Adv. Mech. Des., Syst., Manuf.*, vol. 3, no. 2, pp. 159–170, 2009.

[5] Y. Tang and H. Sasahara, "Analytical prediction of temperature distribution in cylinder liner during various boring operations," *J. Adv. Mech. Des., Syst., Manuf.*, vol. 2, no. 3, pp. 278–289, 2008.

[6] M. Girardi, C. Padovani, D. Pellegrini, and L. Robol, "A finite element model updating method based on global optimization," *Mech. Syst. Signal Process.*, early access, doi: 10.1016/j.ymssp.2020.107372.

[7] M. Nagamatsu, S. Sumida, and A. Nagamatsu, "A new approach on modeling for product development:(The basic concept of functional model)," *Trans. Jpn. Soc. Mech. Eng., C*, vol. 64, no. 622, pp. 1997–2004, 1998.

[8] A. Nagamatsu, S. Sumida, and M. Nagamatsu, "A new approach on modeling for product development: Expansion and unification," *Trans. Jpn. Soc. Mech. Eng., C*, vol. 64, no. 627, pp. 4216–4223, 1998.

[9] S. Hiramatsu, M. Nagamatsu, and S. Sumida, "An approach on modeling for functional development of automobile," SAE Tech. Paper 2000-01-0123, 2000, doi: 10.4271/2000-01-0123.

[10] S. Hiramatsu, S. Sumida, M. Nagamatsu, and A. Nagamatsu, "Modeling for functional expression of rotary apparatus (2nd report, planetary gear train)," *Trans. Jpn. Soc. Mech. Eng., C*, vol. 65, no. 638, pp. 3926–3933, 1999.

[11] S. Sumida and M. Nagamatsu, "A modeling approach on modeling of nonlinear system for functional development of automobile," SAE Tech. Paper 2001-01-0638, 2001, doi: 10.4271/2001-01-0638.

[12] S. Sumida, S. Hiramatsu, and M. Nagamatsu, "Modeling for functional expression of rotary apparatus," SAE Tech. Paper 2002-01-0814, 2002, doi: 10.4271/2002-01-0814.

[13] S. Sumida, S. Hiramatsu, M. Nagamatsu, and A. Nagamatsu, "Modeling for functional expression of rotary apparatus (1st report, clutch and brake)," *Trans. Jpn. Soc. Mech. Eng., C*, vol. 65, no. 635, pp. 2601–2608, 1999.

[14] S. Hiramatsu, S. Sumida, A. Nagamatsu, and H. Arakawa, "Hierarchical functional model for automobile development (2nd report, functional and mechanical models of engine)," *Trans. Jpn. Soc. Mech. Eng., C*, vol. 68, no. 671, pp. 2082–2089, 2002.

[15] S. Hiramatsu, S. Sumida, and A. Nagamatsu, "Hierarchical functional model for automobile development (3rd report, functional model of drivetrain)," *Trans. Jpn. Soc. Mech. Eng., C*, vol. 68, no. 671, pp. 2090–2097, 2002.

[16] Y. Tanabe and S. Sumida, "Evaluation of variance of time history response of the system based on time-constant analysis," *Trans. Jpn. Soc. Mech. Eng.*, vol. 86, no. 887, 2020, Art. no. 2000082.

[17] S. Sato, I. Kajiwara, C. Nishidome, M. Sakata, T. Hatano, and S. Hiramatsu, "Acceleration control of automotive drive system with nonlinearity," in *Proc. MoViC*, Toyohashi, Japan, Aug./Sep. 2017, doi: 10.1299/jsmemovic.2017.15.C13.

[18] R. E. Kalman, "A new approach to linear filtering and prediction problems," *Trans. ASME, J. Basic Eng.*, vol. 82, no. 1, pp. 35–45, 1960.

[19] R. E. Kalman and R. S. Bucy, "New results in linear filtering and prediction theory," *Trans. ASME, J. Basic Eng.*, vol. 83, no. 1, pp. 95–108, 1961.

[20] S. Adachi and I. Maruta, *Fundamentals of Kalman Filter*. Tokyo, Japan: Tokyo Denki Univ. Press, 2012, pp. 96–163.

[21] L. A. McGee and S. F. Schmidt, "Discovery of the Kalman filter as a practical tool for aerospace and industry," NASA, San Francisco, CA, USA, Tech. Memorandum-86847, Nov. 1985.

[22] S. Julier, J. Uhlmann, and H. F. Durrant-Whyte, "A new method for the nonlinear transformation of means and covariances in filters and estimators," *IEEE Trans. Autom. Control*, vol. 45, no. 3, pp. 477–482, Mar. 2000.

[23] Y. Sun, L. Li, B. Yan, C. Yang, and G. Tang, "A hybrid algorithm combining EKF and RLS in synchronous estimation of road grade and vehicle' mass for a hybrid electric bus," *Mech. Syst. Signal Process.*, vols. 68–69, pp. 416–430, Feb. 2016.

[24] S. E. Li, G. Li, J. Yu, C. Liu, B. Cheng, J. Wang, and K. Li, "Kalman filter-based tracking of moving objects using linear ultrasonic sensor array for road vehicles," *Mech. Syst. Signal Process.*, vol. 98, pp. 173–189, Jan. 2018.

[25] D. Li, J. Zhou, and Y. Liu, "Recurrent-neural-network-based unscented Kalman filter for estimating and compensating the random drift of MEMS gyroscopes in real time," *Mech. Syst. Signal Process.*, vol. 147, Jan. 2021, Art. no. 107057.

[26] A. J. Barragan, J. M. Enrique, F. Segura, and J. M. Andujar, "Iterative fuzzy modeling of hydrogen fuel cells by the extended Kalman filter," *IEEE Access*, vol. 8, pp. 180280–180294, 2020.

[27] B. Forrier, F. Naets, and W. Desmet, "Broadband load torque estimation in mechatronic powertrains using nonlinear Kalman filtering," *IEEE Trans. Ind. Electron.*, vol. 65, no. 3, pp. 2378–2387, Mar. 2018.

[28] M. Jama, A. Wahyudie, and S. Mekhilef, "Wave excitation force estimation using an electrical-based extended Kalman filter for point absorber wave energy converters," *IEEE Access*, vol. 8, pp. 49823–49836, 2020.

[29] M. Hehn, E. Sippel, and M. Vossiek, "An iterative extended Kalman filter for coherent measurements of incoherent network nodes in positioning systems," *IEEE Access*, vol. 8, pp. 36714–36727, 2020.

[30] J. Hu, Z. Wang, H. Gao, and L. K. Stergioulas, "Extended Kalman filtering with stochastic nonlinearities and multiple missing measurements," *Automatica*, vol. 48, no. 9, pp. 2007–2015, Sep. 2012, doi: 10.1016/j.automatica.2012.03.027.

[31] H. Liu, F. Hu, J. Su, X. Wei, and R. Qin, "Comparisons on Kalman-Filter-Based dynamic state estimation algorithms of power systems," *IEEE Access*, vol. 8, pp. 51035–51043, 2020.

[32] C. Huang, Z. Wang, Z. Zhao, L. Wang, C. S. Lai, and D. Wang, "Robustness evaluation of extended and unscented Kalman filter for battery state of charge estimation," *IEEE Access*, vol. 6, pp. 27617–27628, 2018.

[33] A. Lagerberg and B. Egardt, "Backlash estimation with application to automotive powertrains," *IEEE Trans. Control Syst. Technol.*, vol. 15, no. 3, pp. 483–493, May 2007.
[34] M. Saito and M. Yamakita, "MPC for a simplified transmission model with backlash using UKF," in *Proc. IEEE Int. Symp. Intell. Control*, Munich, Germany, Oct. 2006, pp. 527–532.
[35] S. Strano and M. Terzo, "Constrained nonlinear filter for vehicle sideslip angle estimation withno a priori knowledge of tyre characteristics," *Control Eng. Pract.*, vol. 71, pp. 10–17, Feb. 2018.
[36] I. Ullah, Y. Shen, X. Su, C. Esposito, and C. Choi, "A localization based on unscented Kalman filter and particle filter localization algorithms," *IEEE Access*, vol. 8, pp. 2233–2246, 2020.
[37] M. S. Challa, J. G. Moore, and D. J. Rogers, "A simple attitude unscented Kalman filter: Theory and evaluation in a magnetometer-only spacecraft scenario," *IEEE Access*, vol. 4, pp. 1845–1858, 2016.
[38] R. Mohammadi Asl, Y. Shabbouei Hagh, S. Simani, and H. Handroos, "Adaptive square-root unscented Kalman filter: An experimental study of hydraulic actuator state estimation," *Mech. Syst. Signal Process.*, vol. 132, pp. 670–691, Oct. 2019.
[39] H. Yonezawa, I. Kajiwara, C. Nishidome, S. Hiramatsu, M. Sakata, and T. Hatano, "Vibration control of automotive drive system with backlash considering control period constraint," *J. Adv. Mech. Des., Syst., Manuf.*, vol. 13, no. 1, pp. 1–15 2019.
[40] H. Yonezawa, I. Kajiwara, S. Sato, C. Nishidome, M. Sakata, T. Hatano, and S. Hiramatsu, "Vibration control of automotive drive system with nonlinear gear backlash," *J. Dyn. Syst., Meas., Control*, vol. 141, no. 12, Dec. 2019, 121002.
[41] J. C. Gerdes and V. Kumar, "An impact model of mechanical backlash for control system analysis," in *Proc. Amer. Control Conf. (ACC)*, Seattle, WA, USA, Jun. 1995, pp. 3311–3315.
[42] M. Nordin, J. Galic', and P.-O. Gutman, "New models for backlash and gear play," *Int. J. Adapt. Control Signal Process.*, vol. 11, no. 1, pp. 49–63, Feb. 1997.
[43] M. Ghandchi-Tehrani, L. I. Wilmshurst, and S. J. Elliott, "Bifurcation control of a duffing oscillator using pole placement," *J. Vib. Control*, vol. 21, no. 14, pp. 2838–2851, Oct. 2015.
[44] C. Moler and C. Van Loan, "Nineteen dubious ways to compute the exponential of a matrix, twenty-five years later," *SIAM Rev.*, vol. 45, no. 1, pp. 3–49, Jan. 2003.

HEISEI YONEZAWA received the B.S. and M.S. degrees in mechanical engineering from Hokkaido University, Japan, in 2017 and 2019, respectively, where he is currently pursuing the Ph.D. degree with the Graduate School of Engineering. His research interests include powertrain control, vibration control, application of Kalman filtering, and sampled-data control. He received the Miura Prize for best students in the field of mechanical engineering from the Japan Society of Mechanical Engineers, in 2019.

ITSURO KAJIWARA received the B.S. degree in engineering from Tokyo Metropolitan University, in 1986, and the M.S. and Ph.D. degrees in engineering from the Tokyo Institute of Technology, in 1988 and 1993, respectively. From 1990 to 2000, he was an Assistant Professor with the School of Engineering, Tokyo Institute of Technology. From 2000 to 2008, he was an Associate Professor with the Graduate School of Engineering, Tokyo Institute of Technology. Since 2009, he has been a Professor with the Graduate School of Engineering, Hokkaido University. His research interests include vibration, control, structural health monitoring, and laser application.

SHOTA SATO received the B.S. and M.S. degrees in mechanical engineering from Hokkaido University, Japan, in 2016 and 2018, respectively. He joined the Integrated Control System Development Division, Mazda Motor Corporation, Hiroshima, Japan, in 2018. He is currently working as a Specialist with Mazda Motor Corporation. His research interests include control of vehicle systems, vibration control, and model predictive control.

CHIAKI NISHIDOME received the B.S. and M.S. degrees in engineering from the Tokyo Institute of Technology, in 2000 and 2002, respectively, and the Ph.D. degree in engineering from Hokkaido University, in 2014. He is currently working at CATEC Inc., Tokyo, Japan. Since 2014, he has been a Manager with the Engineering Department, CATEC Inc. His research interests include vibration control, modal analysis, physical function model, and noise and vibration measurement.

TAKASHI HATANO received the B.S. and M.S. degrees in engineering from Hiroshima University, Japan, in 2005 and 2007, respectively. He jointed Mazda Motor Corporation, Hiroshima, Japan, in 2007. Since 2018, he has been a Senior Specialist with the Integrated Control System Development Division, Mazda Motor Corporation. His research interests include control of vehicle systems, engine control, process control, model predictive control, and PID control. His research has led to ten patents.

SHIGEKI HIRAMATSU received the B.S. degree in engineering from Hokkaido University, Japan, in 1984, and the Ph.D. degree in engineering from the Tokyo Institute of Technology, Japan, in 2003. He jointed Mazda Motor Corporation, Hiroshima, Japan, in 1984. Since 2017, he has been a Senior Principal Engineer with the Integrated Control System Development Division, Mazda Motor Corporation. His research interests include modeling of vehicle systems, physical function model, and model-based development. His research has led to over five articles and one patent.